Colloids and Surfaces B: Biointerfaces 263 (2026) 115592

Contents lists available at ScienceDirect

Colloids and Surfaces B: Biointerfaces

journal homepage: www.elsevier.com/locate/colsurfb

Engineering porous vaterite $CaCO_3$ nanostructures via alcohol–surfactant coordination in co-precipitation: A facile route to tunable drug-carrier platforms

Seung-Yeon Kim [a,b,1], Min-Kyung Kang [a,c,1], A.-Ran Min [a,c], Jin-Woo Jeong [a,c], A.-Jin Kim [a,d], Chansu Park [c], Kangwon Lee [b,*], Young-Ran Lee [a,*], Seong-Joong Kim [a,*]

[a] Bio-Convergence R&D Division, Korea Institute of Ceramic Engineering and Technology (KICET), 202 Osongsaengmyeong 1-ro, Osong-eup, Heungdeok-gu, Cheongju-si, Chungcheongbuk-do, Republic of Korea
[b] Graduate School of Convergence Science and Technology, Seoul National University, Gwanak-ro, Gwanak-gu, Seoul 08826, Republic of Korea
[c] College of Pharmacy, Chungbuk National University, 194-21 Osongsaengmyeong 1-ro, Osong-eup, Heungdeok-gu, Cheongju-si, Chungcheongbuk-do, Republic of Korea
[d] Chemical and Biomolecular Engineering, Yonsei University, 50 Yonsei-ro Seodaemun-gu, Seoul 03722, Republic of Korea

ARTICLE INFO

Keywords:
Porous vaterite $CaCO_3$ nanoparticles
Co-precipitation
Alcohol–surfactant coordination
Drug delivery
Antigen adsorption

ABSTRACT

Calcium carbonate ($CaCO_3$) is widely studied for drug delivery because of its excellent biocompatibility, low toxicity, and the high surface area and porosity of its vaterite phase, which enable efficient drug loading and cellular uptake. However, the intrinsic metastability of vaterite leads to its transformation into stable calcite, which limits its practical applications. In this study, porous vaterite $CaCO_3$ nanoparticles were synthesized through a facile co-precipitation process assisted by alcohols and surfactants, which regulate ion diffusion and control the crystallization pathway. The effects of the alcohol type and concentration, as well as the surfactant mixing ratio, were systematically investigated to optimize the particle size, morphology, and phase composition. The synergistic regulation of solvent polarity and surfactant balance enabled the formation of uniform vaterite nanoparticles (~300 nm) with high porosity and specific surface area (89.3 m^2/g). Ovalbumin—a model antigen—was adsorbed onto the porous nanoparticles with an efficiency of > 99.1%. Moreover, *in vitro* cytotoxicity and antigen-presentation assays demonstrated excellent biocompatibility (cell viability >90%) and enhanced IL-2 secretion (~2200 pg/mL), indicating potent immunostimulatory capability. The findings demonstrate that the alcohol-surfactant-assisted co-precipitation strategy provides a simple yet effective route for the controlled synthesis of stable, porous vaterite $CaCO_3$ nanoparticles. These nanostructures exhibit considerable potential as biocompatible carriers for antigen delivery, drug loading, and other advanced biomedical applications.

1. Introduction

Calcium carbonate ($CaCO_3$) is a representative inorganic material that has been widely investigated owing to its excellent biocompatibility, low toxicity, and high solubility [1–4]. It has been explored across various fields, including drug delivery, tissue engineering, environmental applications, and cosmetics [5–10]. Porous $CaCO_3$ is a promising platform for drug-delivery systems because it enables the effective control of drug loading and release rates [11,12]. Other representative inorganic carriers, such as silica, gold, and calcium phosphate, can also provide high biocompatibility [13–17]. However, they have the limitations of low biodegradability, high cost, and possible accumulation in the body [18–20]. In contrast, $CaCO_3$ is cost-effective and biodegradable at physiological pH, facilitating drug release through natural decomposition [20].

$CaCO_3$ consists of three crystalline phases: calcite, aragonite, and vaterite. It is difficult to control the dissolution rate of the calcite and aragonite phases owing to their high structural stability [21,22]. In contrast, the vaterite phase has a high surface area and porous structure, which improves drug-loading efficiency and cellular uptake [23,24]. However, the metastable vaterite phase tends to be converted into the thermodynamically more stable calcite phase under aqueous conditions [25,26]. In addition to the crystalline phase, the particle size of $CaCO_3$ plays an important role in drug delivery. $CaCO_3$ particles larger than 1

* Corresponding authors.
E-mail addresses: kangwonlee@snu.ac.kr (K. Lee), yrlee@kicet.re.kr (Y.-R. Lee), sjkim@kicet.re.kr (S.-J. Kim).
[1] Seung-Yeon Kim and Min-Kyung Kang contributed equally to this study.

https://doi.org/10.1016/j.colsurfb.2026.115592
Received 9 December 2025; Received in revised form 11 February 2026; Accepted 2 March 2026
Available online 3 March 2026

μm in cells have limited intracellular uptake and may be rapidly removed by macrophages. Therefore, nanoparticles smaller than 500 nm are considered more suitable for drug delivery, as their small size helps reduce side effects by facilitating intracellular uptake and rapid degradation [27]. Thus, it is critical to synthesize and maintain the $CaCO_3$ nanoparticles of the vaterite phase for application in drug delivery.

Several methods have been used to prepare $CaCO_3$ nanoparticles, such as emulsion, gas diffusion, and co-precipitation [28–33]. The emulsion process enables the $CaCO_3$ to form uniform nanoparticles during reaction at the oil–water interface. The particle size and distribution are controlled via the addition of surfactants and emulsifiers [34]. The gas-diffusion method forms the $CaCO_3$ nanoparticles via the reaction of Ca^{2+} and CO_3^{2-}, which is produced by the decomposition of ammonium carbonate. However, long reaction times, use of organic solvents, and high energy consumption make them less suitable for large-scale production of $CaCO_3$ [35]. In contrast, co-precipitation is the most widely used method because of its simplicity and scalability. Nevertheless, the high reaction rate of the aqueous-based co-precipitation process makes it difficult to control the particle size and morphology of $CaCO_3$. Typically, calcite $CaCO_3$ microparticles are formed, which are not suitable for drug delivery.

To overcome these limitations, many studies have focused on controlling the reaction parameters, such as the precursor concentration, reaction temperature, stirring speed, and additives [36–39]. Persano et al. studied the effects of the precursor salt concentration and reaction temperature on the particle size of $CaCO_3$ during co-precipitation [37]. High salt concentrations led to rapid growth and aggregation, whereas moderate salt concentrations facilitated the formation of uniformly spherical nanoparticles. High reaction temperatures increased the nucleation frequency, resulting in smaller particles and easier formation of the vaterite phase [37,40]. In contrast, low temperatures promoted the formation of large calcite particles by accelerating crystal growth [26]. Yohta Mori et al. demonstrated that different stirring processes could determine the crystal phase and shape during the mixing of calcium chloride ($CaCl_2$) and potassium carbonate (K_2CO_3) in an aqueous solution [41]. Yan et al. controlled the particle size and distribution by varying the stirring speed [42]. Daud et al. demonstrated that high-speed stirring using a multi-impeller system is effective for forming spherical vaterite nanoparticles [43]. Ethylene glycol and glycerol were added to increase the solution viscosity and reduce ion diffusion [44,45]. This slowed crystallization and promoted the formation of the vaterite phase. In addition, surfactants such as sodium dodecyl sulfate and Pluronic F127 have been added to ethanol–water mixtures, facilitating control of the crystal phase and the formation of spherical, flower-like, and rod-like structures [46]. However, controlling nucleation and growth precisely and ensuring the long-term dispersion stability of the particles cannot be fully achieved by adding viscosity modifiers or surfactants [47]. Thus, further investigation is required.

Studies have indicated that the solvent mixture affects the crystal phase and dispersibility of $CaCO_3$ particles [48–50]. Zhang et al. delayed the nucleation rate via slow solvation of Ca^{2+} and CO_3^{2-} ions in an ethanol/water mixture, which tended to form the more stable vaterite phase [51]. Giulia et al. formed a vaterite phase using various alcohol and salt concentrations. These studies suggest that alcohol-based solvents can control vaterite-phase formation [52]. Nevertheless, there is a lack of effort to reduce the particle size and improve dispersibility. Further studies are needed to address these issues.

In this study, $CaCO_3$ nanoparticles of the stable vaterite phase were synthesized via co-precipitation. Various alcohols were used as solvents in water to control particle size and crystal phase. Based on the addition of alcohols, the effect of the reaction rate on particle formation was investigated. In addition, nonionic surfactants such as Span 80 and Tween 40 were added to the alcohol–water mixture to improve the dispersibility of the nanoparticles. This approach can simultaneously achieve nanoparticle size and improve the dispersity of $CaCO_3$. Previously, Span 80 and Tween 40 were used only in emulsion methods. As the precipitation method is performed in water, its use in this approach has not yet been reported. Therefore, this is the first study to explore the use of Span 80 and Tween 40 in combination with alcohols for precipitation synthesis. Furthermore, the biomedical potential of the synthesized porous $CaCO_3$ nanoparticles was evaluated using ovalbumin (OVA) as a model antigen. By providing high antigen-loading capacity, controlled release behavior, and efficient cellular interaction, the $CaCO_3$ nanoparticles function as an antigen delivery carrier with adjuvant-like effects, leading to enhanced immune responses without inducing significant cytotoxicity.

2. Experimental

2.1. Materials

Calcium chloride ($CaCl_2$), sodium carbonate (Na_2CO_3), OVA, Tween 40 (Polyoxyethylene sorbitan monopalmitate), Span 80 (Sorbitan monooleate), and alcohol-based solvents, including methanol, ethanol, 2-propanol, 1-butanol, and 1-pentanol, were obtained from Sigma-Aldrich (USA) and used without further purification. The BCA (Bicinchoninic Acid) protein assay kit (Pierce™, USA) was employed to determine the loading efficiency. The EZ-Cytox kit (DOGEN Bio, Korea) was used to assess cell cytotoxicity. The Mouse IL-2 ELISA kit (BD OptEIA™, USA) was used to evaluate the antigen-presentation efficiency.

2.2. Cell lines

DC2.4 and CD8OVA cell lines were purchased from the Korean Cell Line Bank (KCLB, Korea). The cells were cultured in Dulbecco's Modified Eagle Medium (D-Glucose 4.5 g/L, 25 mM HEPES) supplemented with 10% fetal bovine serum (Gibco, USA), 100 U/mL penicillin, and 100 U/mL streptomycin at 37 °C in a humidified incubator with 5% CO_2.

2.3. Preparation of porous $CaCO_3$ nanoparticles

Porous $CaCO_3$ nanoparticles were synthesized using a co-precipitation method (Figure S1). A 0.01 M $CaCl_2$ solution was prepared in 10 mL of distilled water and vortexed for 1 min at room temperature to ensure complete dissolution. Separately, surfactants (Tween 40 and Span 80) at various ratios were mixed with alcohols, such as methanol, ethanol, propanol, butanol, and pentanol. The amounts of surfactants and alcohols were adjusted in the ranges of 50–200 μL and 1–10 mL, respectively. The mixture was vortexed for 30 s to achieve homogeneous dispersion and then added to the 0.01 M $CaCl_2$ solution, followed by homogenization at 5000 rpm for 10 min. Subsequently, 10 mL of a 0.01 M Na_2CO_3 solution was added, and the mixture was homogenized again at 5000 rpm for 10 min to promote the reaction between Ca^{2+} and CO_3^{2-}. The optimization of the homogenization speed and molar ratio is shown in Figures S2 and S3, respectively. After the reaction, the suspension was centrifuged at 5000 rpm for 10 min to collect the $CaCO_3$ precipitate. The precipitate was washed three times with ethanol to remove any residual impurities. The $CaCO_3$ particles were finally obtained via drying in an oven at 70 °C for 12 h. The detailed synthesis conditions are presented in Table S1.

2.4. OVA adsorption onto $CaCO_3$ nanoparticles

OVA was employed as a model antigen to demonstrate the superiority of the synthesized $CaCO_3$ nanoparticles as drug-delivery agents. For the adsorption of OVA onto $CaCO_3$ nanoparticles, an OVA solution was prepared at a concentration of 10 mg/mL, and 10 mg of $CaCO_3$ nanoparticles was added to 1 mL of the OVA solution. The mixture was vigorously stirred at room temperature for 12 h to allow sufficient adsorption of OVA onto the porous $CaCO_3$ nanoparticles. After adsorption, the OVA-$CaCO_3$ mixture was centrifuged, and the supernatant was

collected. To completely recover residual OVA from the $CaCO_3$ nanoparticles, the precipitated nanoparticles were resuspended in phosphate-buffered saline (PBS) and washed again via centrifugation. The washing solutions were combined with the collected supernatants. The total amount of OVA in the combined solution was quantified via the BCA assay, which was used to determine the adsorption efficiency of OVA onto the $CaCO_3$ nanoparticles. All experiments were performed independently three times.

2.5. In vitro cytotoxicity evaluation of OVA@$CaCO_3$ nanoparticles

The cytotoxicity of OVA@$CaCO_3$ (denoted as OVA-adsorbed $CaCO_3$) nanoparticles was evaluated using the CCK-8 assay. Mouse-derived dendritic cell lines (DC2.4, 4×10^4 cells/well) were seeded into 96-well plates and stabilized for 18 h at 37 °C in a humidified incubator with 5% CO_2. $CaCO_3$ nanoparticles were diluted to final concentrations of 4, 2, 1, 0.5, 0.25, 0.125, 0.063, and 0.031 mg/mL (based on OVA content), and the cells were treated with the nanoparticles for 2 h. After treatment, the nanoparticles were removed, and the cells were washed twice with PBS to eliminate residual formulations. Subsequently, 200 μL of 10% CCK-8 solution diluted by cell culture medium was added to each well, followed by incubation for 1 h at 37 °C with 5% CO_2. The plates were then centrifuged at 3500 rpm for 5 min, and the supernatants were collected. The absorbance was measured at 450 nm using a microplate spectrophotometer (Spectra Max ABS, USA).

2.6. Antigen-presentation efficiency of OVA@$CaCO_3$ nanoparticles

To evaluate the antigen presentation of $CaCO_3$ nanoparticles, mouse-derived dendritic cells that had phagocytosed the nanoparticles were co-cultured with CD8OVA cells, and the amount of IL-2 secreted by CD8OVA cells was measured.

DC2.4 (4×10^4 cells/well) were seeded into 96-well plates and stabilized for 18 h at 37 °C in a humidified incubator with 5% CO_2. $CaCO_3$ nanoparticles were diluted to final concentrations of 4, 2, 1, 0.5, 0.25, 0.125, 0.063, and 0.031 mg/mL (based on OVA content) and incubated with DC2.4 cells for 2 h. After treatment, the nanoparticles were removed, and the cells were washed twice with PBS to eliminate residual formulations. CD8OVA cells (2×10^5 cells/well) were added and co-cultured with DC2.4 for 18 h under the same conditions. Culture supernatants were collected after centrifugation at 3500 rpm for 5 min, and IL-2 secretion from CD8OVA cells was quantified using an IL-2 ELISA kit (BD Biosciences, USA).

2.7. Time-dependent OVA release of OVA@$CaCO_3$ nanoparticles

To investigate the time-dependent release profile of OVA, $CaCO_3$ particles containing OVA at a 1:1 ratio (1 mg:1 mg) were tested under different pH (5.0 and 7.4) and temperature (4 and 25 °C) conditions. A 45 mL sample was divided equally into two 22.5 mL conical tubes and centrifuged at 4000 rpm for 10 min to remove the supernatant. Each pellet was resuspended in 22.5 mL of PBS adjusted to pH 5.0 or 7.4. The resulting suspensions were then aliquoted into four 10 mL tubes to establish four experimental conditions: pH 5–4 °C, pH 5–25 °C, pH 7.4–4 °C, and pH 7.4–25 °C. The samples were gently mixed without vortexing to ensure homogeneous dispersion. From each tube, 500 μL samples were collected, transferred into microtubes, and centrifuged at 15,000 rpm for 10 min. The supernatants were collected as Day 0 samples and stored. This sampling procedure was repeated daily up to Day 7, after which the supernatants were analyzed using a BCA assay to quantify the released OVA.

2.8. Characterization

The morphology and elemental distribution of the $CaCO_3$ particles were analyzed using a scanning electron microscope (SEM, COXEM-EM30N and Tescan VEGA-II LSU for high-resolution) and an energy dispersive X-ray spectroscope (EDS). The emulsions formed by the addition of butanol and pentanol to the $CaCl_2$ aqueous solution were observed under an optical microscope (OM, Primovert, ZEISS). The size distribution of the synthesized $CaCO_3$ particles was confirmed using dynamic light scattering (DLS, Malvern Zetasizer) and it was performed independently three times. For the DLS analysis, 1 mL of distilled water was mixed with 5 mg of particles in a cuvette to achieve uniform dispersion prior to measurement. The surface charges of the OVA, $CaCO_3$, and OVA@$CaCO_3$ particles were evaluated via zeta-potential analysis using the same DLS instrument. The chemical structures of OVA, $CaCO_3$, and OVA@$CaCO_3$ particles were investigated through Fourier transform infrared (FT-IR) spectroscopy in the attenuated total reflectance mode (SP8000, PerkinElmer) over the range of 4000–600 cm^{-1} . The thermal behavior of the $CaCO_3$ and OVA@$CaCO_3$ particles was examined via thermogravimetric analysis (TGA, SDT Q600). Approximately 25 mg of each sample was heated in a platinum crucible from room temperature to 800 °C at a rate of 10 °C/min under air flow. The weight loss was analyzed to confirm the adsorption of OVA onto the $CaCO_3$ particles. The crystalline properties of the synthesized $CaCO_3$ were examined via X-ray diffraction (XRD) using a Rigaku D/Max-2200V diffractometer equipped with a Cu source and a graphite monochromator at 40 kV. XRD was used to distinguish between the vaterite and calcite phases. The porous structure of the $CaCO_3$ particles was confirmed by nitrogen adsorption–desorption measurements using a Brunauer–Emmett–Teller (BET) surface area analyzer (Micromeritics ASAP 2460). In addition, the pore-size distribution was calculated from Barrett–Joyner–Halenda desorption data. The internal morphology and microstructure of the $CaCO_3$ particles were further examined using a Cs-corrected transmission electron microscope (TEM; JEM-ARM200F (NEOARM), JEOL) operated at 200 kV and equipped with a STEM-Cs corrector. The cytotoxicity of OVA@$CaCO_3$ toward dendritic cells was assessed via Live/Dead assay using a fluorescent microscope (EVOS™ M5000 Imaging System, Invitrogen))

3. Results and discussion

3.1. Optimization of synthesis conditions for $CaCO_3$ nanoparticles

3.1.1. Effect of alcohol type on formation of $CaCO_3$ nanoparticles

Fig. 1 presents scanning electron microscopy (SEM) images of $CaCO_3$ particles synthesized in the presence of different alcohols. Fig. 1(a) shows pristine $CaCO_3$ prepared without alcohol, and Figs. 1(b)–(f) show $CaCO_3$ prepared with methanol, ethanol, propanol, butanol, and pentanol, respectively. $CaCO_3$ synthesized in aqueous solution typically forms the stable calcite phase, which has a hexagonal structure and is several micrometers in size [53]. In this study, a similar trend was observed, with hexagonal crystals of 3–5 μm (Fig. 1(a)). The high polarity and strong ion dissociation in water supply sufficient Ca^{2+} and CO_3^{2-} ions, favoring crystal growth over nucleation. In contrast, alcohol-assisted synthesis led to the formation of spherical $CaCO_3$ particles with only a few cubic crystals. The particle size can be tuned by employing alcohols with different numbers of carbon atoms. $CaCO_3$ synthesized with methanol and ethanol exhibited particle sizes of 4 and 3 μm, respectively, as indicated by the SEM images (Figs. 1(b) and (c)) and DLS results (Fig. 1(g)). In propanol and butanol, the particle sizes decreased significantly to 400 and 735 nm, respectively. The addition of propanol resulted in the formation of the smallest and most uniform nanoparticles. However, in the case of pentanol, the particle size increased to 3 μm, with a broad size distribution.

Methanol (C1), ethanol (C2), and propanol (C3) were miscible in water (Table S2). The addition of alcohol reduces the polarity of the aqueous solution, thereby limiting the availability of Ca^{2+} and CO_3^{2-} and suppressing particle growth [51]. However, relatively polar alcohols, such as methanol and ethanol, did not significantly reduce the polarity of the aqueous medium, indicating that ion diffusion was maintained at

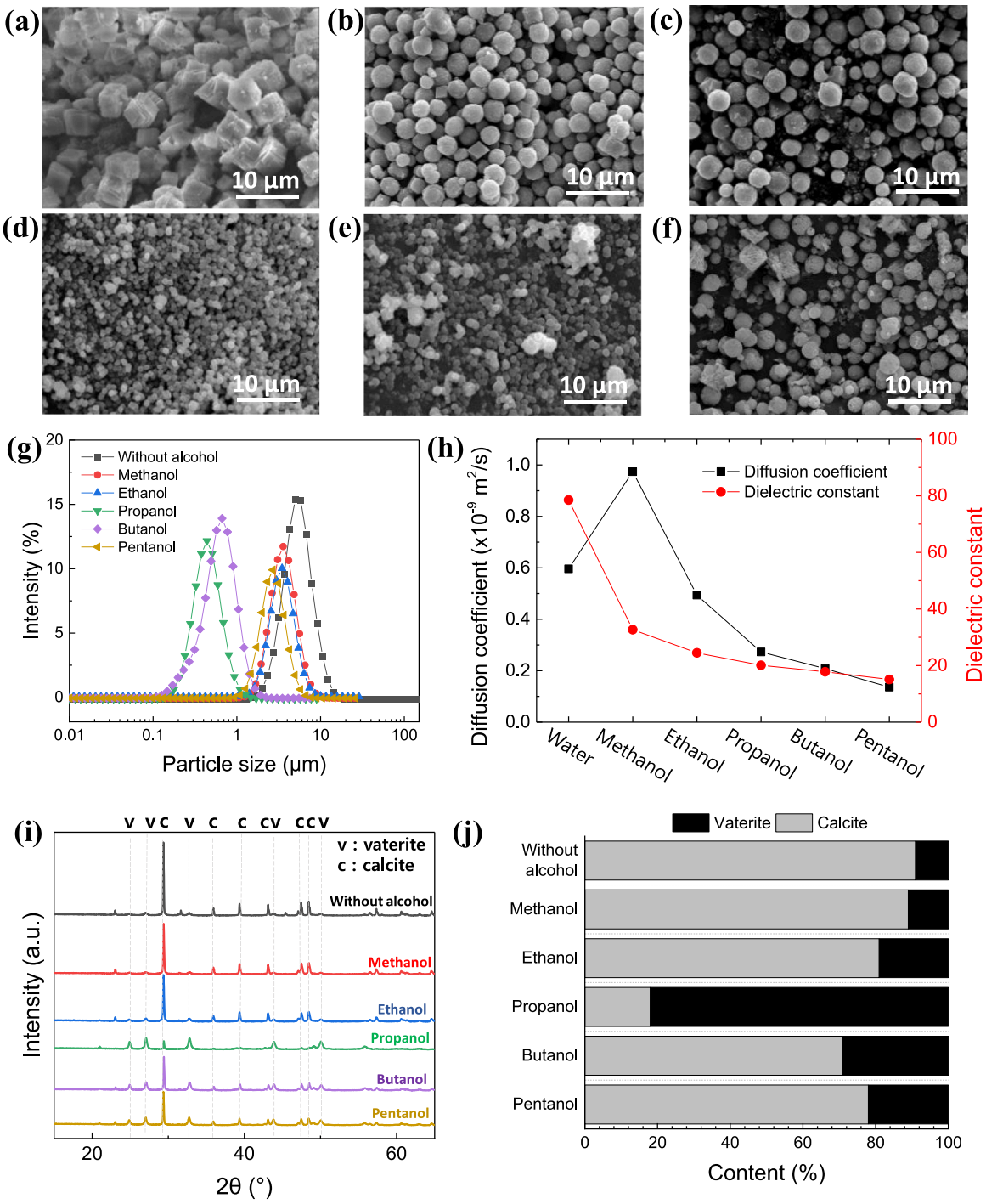

Fig. 1. Characterization of $CaCO_3$ particles synthesized with various alcohols. (a-f) SEM images: (a) without alcohol, (b) methanol, (c) ethanol, (d) propanol, (e) butanol, and (f) pentanol. (g) Particle size distributions. (h) Diffusion coefficient and dielectric constant. (i) XRD patterns and (j) phase contents.

high levels (Fig. 1(h) and Table S3). Although methanol exhibits a lower viscosity than water, its significantly lower dielectric constant limits ion dissociation. Consequently, although diffusion may proceed slightly faster, the overall reaction kinetics remain slightly slower than those in aqueous media. Therefore, in the presence of methanol and ethanol, crystal growth dominated nucleation, leading to the formation of large microparticles. Nevertheless, their size was smaller than that of the particles synthesized without alcohol. In contrast, propanol reduces the polarity of the aqueous solution to a greater extent than either methanol or ethanol. This decreases the diffusivity and activity of Ca^{2+} and CO_3^{2-} ions [54]. Indeed, FT-IR analysis and pH measurement results showed that the degree of ionization of ion species decreased with the addition of propanol (Figure S4 and Table S4). As a result, the effective supersaturation ($S = [Ca^{2+}]\,[CO_3^{2-}]/K_{sp}$) increases even at the same ion concentration. According to classical nucleation theory, the nucleation barrier (ΔG^*) is strongly dependent on supersaturation and decreases rapidly with increasing supersaturation ($\Delta G^* \propto (\ln S)^{-2}$), thereby promoting nucleation, as detailed in the Supplementary materials (Eq. 2). In the presence of propanol, the dielectric constant of the reaction medium decreases, reducing the equilibrium solubility of Ca^{2+} and CO_3^{2-} ions and thereby increasing the effective supersaturation (S). As a result, the nucleation barrier is lowered, favoring the formation of numerous nuclei

[55]. At the same time, the reduced dielectric constant decreases ion diffusivity (Fig. 1h and Table S3), which limits diffusion-driven crystal growth. As a result, the system shifts to a nucleation-dominated process, yielding uniformly sized $CaCO_3$ nanoparticles.

Butanol (C4) and pentanol (C5) had relatively low solubility of 7.0 and 2.7 g per 100 g water, respectively. In this study, 1 mL of alcohol was added to 10 mL of $CaCl_2$ aqueous solution, resulting in the formation of emulsions. Optical images of the solutions containing butanol and pentanol (Figure S5) show emulsions of ~1 and 1–3 μm, respectively. The emulsion interface between the alcohol and water has an intermediate polarity owing to the existence of OH groups and alkyl chains in the alcohol molecules, making it neither fully hydrophilic nor hydrophobic. Furthermore, the addition of low-solubility alcohols reorganizes the hydration structure, including the water density, molecular orientation, and hydrogen-bonding networks. At the emulsion interface, the relatively low dielectric environment temporarily concentrates Ca^{2+} and CO_3^{2-} ions. Consequently, nucleation occurs preferentially at the interface rather than in the bulk solution. However, because the number of nuclei formed in the emulsion interface is limited, the existing nuclei undergo sufficient growth, leading to the formation of $CaCO_3$ microparticles despite the very low diffusion coefficient and dielectric constant (Fig. 1(f)). In the case of butanol, the number of emulsions formed in water is smaller than that formed in pentanol because of its higher solubility. Moreover, when 10 mL of a Na_2CO_3 aqueous solution was added to the butanol/$CaCl_2$ mixture, the butanol emulsions disappeared as they dissolved in water, exceeding the solubility limit of butanol. Therefore, as shown in Fig. 1(e), $CaCO_3$ synthesized in the presence of butanol consisted of both nanoparticles and microparticles.

Overall, the addition of alcohols influenced the particle size and distribution of $CaCO_3$ by (i) altering the solvent polarity and ion diffusivity, which modulated the supersaturation and nucleation rates, and (ii) forming emulsions in low-solubility alcohols that created localized supersaturation and diffusion-limited environments, shifting the nucleation–growth balance (Fig. 2).

Figs. 1.(i) and (j) shows the XRD patterns of $CaCO_3$ synthesized with different alcohols. Vaterite is structurally suitable for applications that require high porosity and biodegradability. However, because it readily transforms into the thermodynamically stable calcite phase, precise control during its synthesis is necessary [21]. The addition of methanol and ethanol during $CaCO_3$ synthesis resulted in high calcite contents of 89 and 81%, respectively. The high polarity of these solvents maintains ion solubility and mobility, which promotes the rapid crystal growth and stabilization of calcite. For propanol, the vaterite content rapidly increased to 82%, with a remarkable reduction in calcite. The lower polarity of propanol reduces the diffusivity of Ca^{2+} and CO_3^{2-}, inducing supersaturation. This suppresses crystal growth and inhibits phase conversion to calcite during $CaCO_3$ synthesis. Conversely, the addition of butanol and pentanol significantly reduced the vaterite content to 29 and 22%, respectively. As shown in Figure S5, their low solubility led to emulsion formation, which caused localized supersaturation and diffusion-limited environments at the emulsion interface. This restriction on the number of nuclei and induced crystal growth led to transformation into the stable calcite phase.

3.1.2. *Effect of propanol concentration on formation of $CaCO_3$ nanoparticles*

Figs. 3(a-d) shows SEM images of the $CaCO_3$ particles prepared with various amounts of propanol. When 0.5 mL of propanol was added (Fig. 3 (a)), hexagonal particles with sizes of 3–5 μm were observed, similar to those prepared without alcohol (Fig. 1(a)). This suggests that adding < 0.5 mL of propanol is ineffective for tuning $CaCO_3$ particle morphology. In contrast, $CaCO_3$ synthesized using 1 mL of propanol exhibited uniform spherical nanoparticles. An appropriate amount of propanol reduced the polarity of the solution, thereby reducing ion dissociation and the concentration of free ions [56]. In this study, reduced ion dissociation delayed ionic bonding between Ca^{2+} and CO_3^{2-}, which promoted nucleation over crystal growth. As a result, spherical nanoparticles were selectively formed via a kinetically favorable pathway. With larger amounts of propanol (5 and 10 mL), the particle size increased. When an excessive amount of propanol was added, the polarity of the solution was severely reduced, restricting ion mobility and bonding reactions. Consequently, crystal growth became dominant, leading to the formation of nonuniform $CaCO_3$ particles. Furthermore, as shown in Table S5, the reaction yield decreased with an increasing propanol concentration. This indicated that the interaction between Ca^{2+} and CO_3^{2-} ions was hindered.

Fig. 3(e) shows the particle-size distribution of $CaCO_3$ prepared with different amounts of propanol. The average size of the particles synthesized with propanol (0.5 mL) decreased slightly compared to that of the original $CaCO_3$. The addition of 1 mL of propanol significantly reduced the average particle size to ~400 nm, accompanied by a narrow size distribution. This result was consistent with the SEM image shown in Fig. 3(b). When 5 mL of propanol was added, two distinct particle populations appeared around 400 nm and 1 μm. As mentioned previously, higher propanol concentrations gradually suppress nucleation while favoring crystal growth. Therefore, both nucleation and growth are competitively influenced by these conditions, leading to the coexistence of $CaCO_3$ nano- and microparticles. With 10 mL of propanol, crystal growth dominated over nucleation, resulting in larger particles of

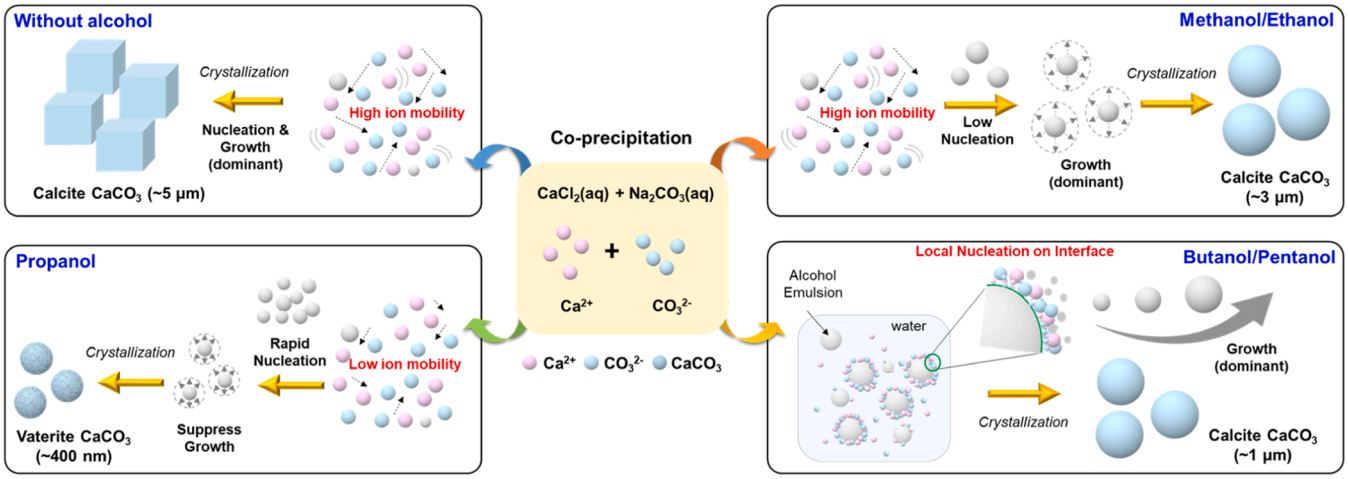

Fig. 2. Illustration of the $CaCO_3$ synthesis mechanism depending on the type of alcohol.

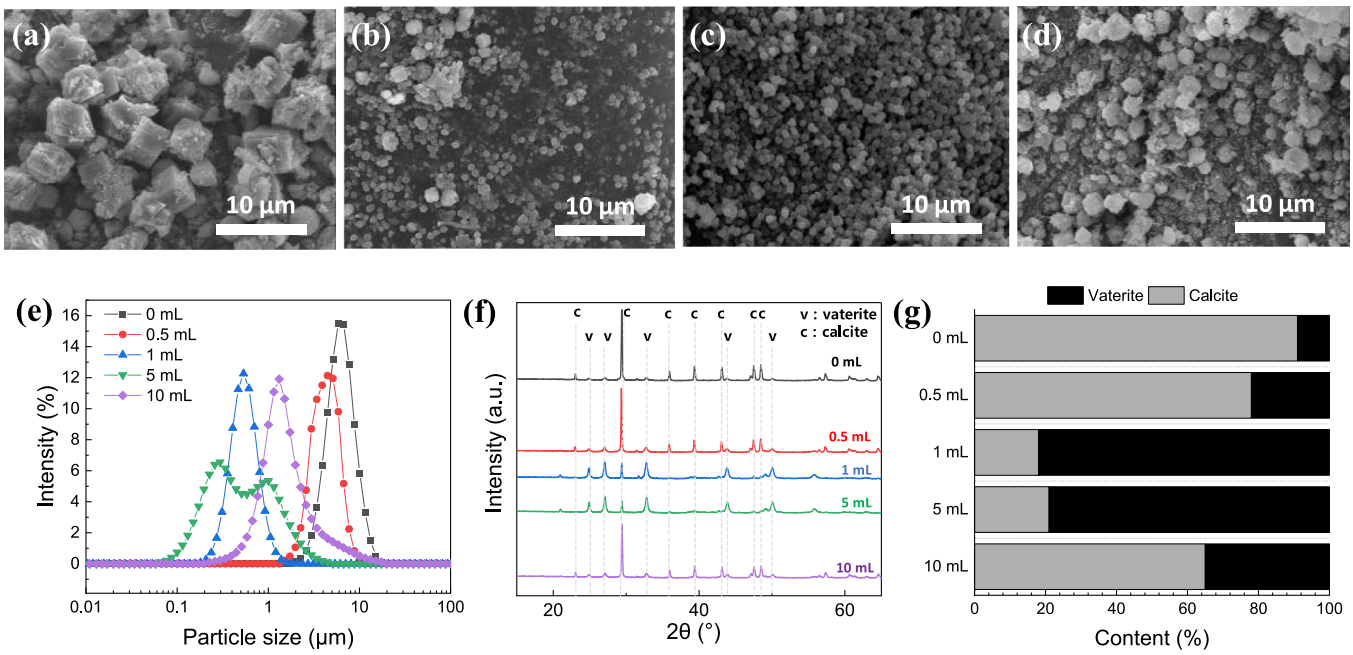

Fig. 3. Characterization of $CaCO_3$ particles synthesized with various propanol concentrations. (a-d) SEM images: (a) 0.5, (b) 1, (c) 5, and (d) 10 mL. (e) Particle size distributions. (f) XRD patterns and (g) phase contents.

~1 μm and a broader size distribution.

Figs. 3(f) and (g) present the XRD patterns and phase contents of $CaCO_3$ synthesized with different amounts of propanol. With 0.5 mL of propanol, the fraction of the vaterite phase increased by approximately 10%, although calcite remained the dominant phase. The addition of 1 mL of propanol significantly increased the vaterite content. This corresponded to the formation of small spherical nanoparticles, as indicated by the SEM and DLS results in Figs. 3(a-e). This behavior is attributed to the rapid termination of nucleation and growth caused by the balanced ion dissociation, as discussed above. When the propanol content was increased to 5 mL, the vaterite phase remained dominant despite slight particle growth (Fig. 3(c)).

However, for $CaCO_3$ prepared with 10 mL of propanol, the calcite content increased again. In this case, the particle size increased, and the size distribution broadened (Figs. 3(d) and 3(e)). Although the polarity was further reduced at high propanol concentrations (10 mL), the calcite fraction increased. This behavior is attributed to changes in the microstructure of the reaction solution, leading to the formation of an emulsion-like microenvironment in the aqueous phase [57]. Such a heterogeneous environment generates local concentration gradients, where crystal growth and recrystallization become more dominant than nucleation. Consequently, excessive polarity reduction promotes the transformation of metastable vaterite into thermodynamically stable calcite.

Based on the combined analysis of particle morphology, size distribution, and phase composition, the addition of 1 mL of propanol was identified as the optimal condition for synthesizing uniform $CaCO_3$ nanoparticles with a predominant vaterite phase.

3.1.3. *Effect of surfactant ratio on formation of $CaCO_3$ nanoparticles*

Figs. 4(a-f) shows SEM images and DLS results of $CaCO_3$ nanoparticles prepared with different Span 80:Tween 40 ratios. Most studies on the synthesis of $CaCO_3$ nanoparticles via the emulsion method with surfactants have focused on controlling particle size and morphology through interfacial stabilization [58,59], whereas the co-precipitation method with surfactants has been rarely reported, owing to the lack of a distinct water–solvent interface. In this study, $CaCO_3$ nanoparticles were synthesized using hydrophilic and hydrophobic surfactants during a co-precipitation process, in which the addition of alcohol controlled the reaction rate.

Figs. 4(a) and (b) present SEM images of $CaCO_3$ prepared with Span 80 and Tween 40, respectively, both showing irregularly aggregated particles. In addition, the DLS results in Fig. 4(f) indicate broad size distributions ranging from a few micrometers to several hundred micrometers. As shown in Figure S6, the hydrophobic Span 80, which consists of sorbitan rings and long hydrocarbon chains, can inhibit crystal growth via adsorption onto the particle surface. Nevertheless, this reduces the surface stability and enhances interparticle attraction, leading to aggregation. Tween 40 can efficiently disperse Ca^{2+} and CO_3^{2-} ions through its polyethylene glycol chains, resulting in the formation of numerous small nuclei. However, surface interactions such as hydrogen bonding and van der Waals forces cause particle aggregation. Consequently, when either surfactant is used, aggregated particles are formed.

$CaCO_3$ synthesized with 2:8 and 8:2 Tween 40 mixtures exhibited smaller and more uniform nanoparticles, respectively, as shown in Figs. 4(c) and (d). The combination of Span 80 and Tween 40 facilitated nucleation while suppressing further growth. The coexistence of hydrophilic and hydrophobic chains on the particle surfaces inhibited aggregation by providing steric hindrance and enhancing electrostatic repulsion. Nevertheless, partially aggregated particles were observed in the SEM images, and the size distribution in the DLS results was similar to that of the particles synthesized without surfactants.

Fig. 4(e) is SEM image of $CaCO_3$ nanoparticles synthesized at 5:5 ratio of Span 80:Tween 40 surfactants. The smallest particle size of approximately 300 nm was observed with a narrow distribution in the SEM image and DLS results. The formation of smaller and more uniform $CaCO_3$ nanoparticles is primarily associated with the reduced ionization of ion species (Figure S4 and Table S4) and the optimized hydrophile–lipophile balance (HLB) achieved by the mixed Span 80/Tween 40 system (Table S6), respectively. The optimized HLB value provides effective steric stabilization and enhanced electrostatic repulsion, thereby suppressing particle aggregation. Therefore, the complementary effect of the Span 80 and Tween 40 surfactants on the nanoparticle surfaces enabled the production of the smallest and most uniform $CaCO_3$ nanoparticles by achieving balanced control of nucleation and growth. Meanwhile, the optimal particle size and distribution were obtained with a surfactant amount of 100 μL (Figure S7). Thus, the combination of Span 80 and Tween 40 served as a key factor in balancing nucleation,

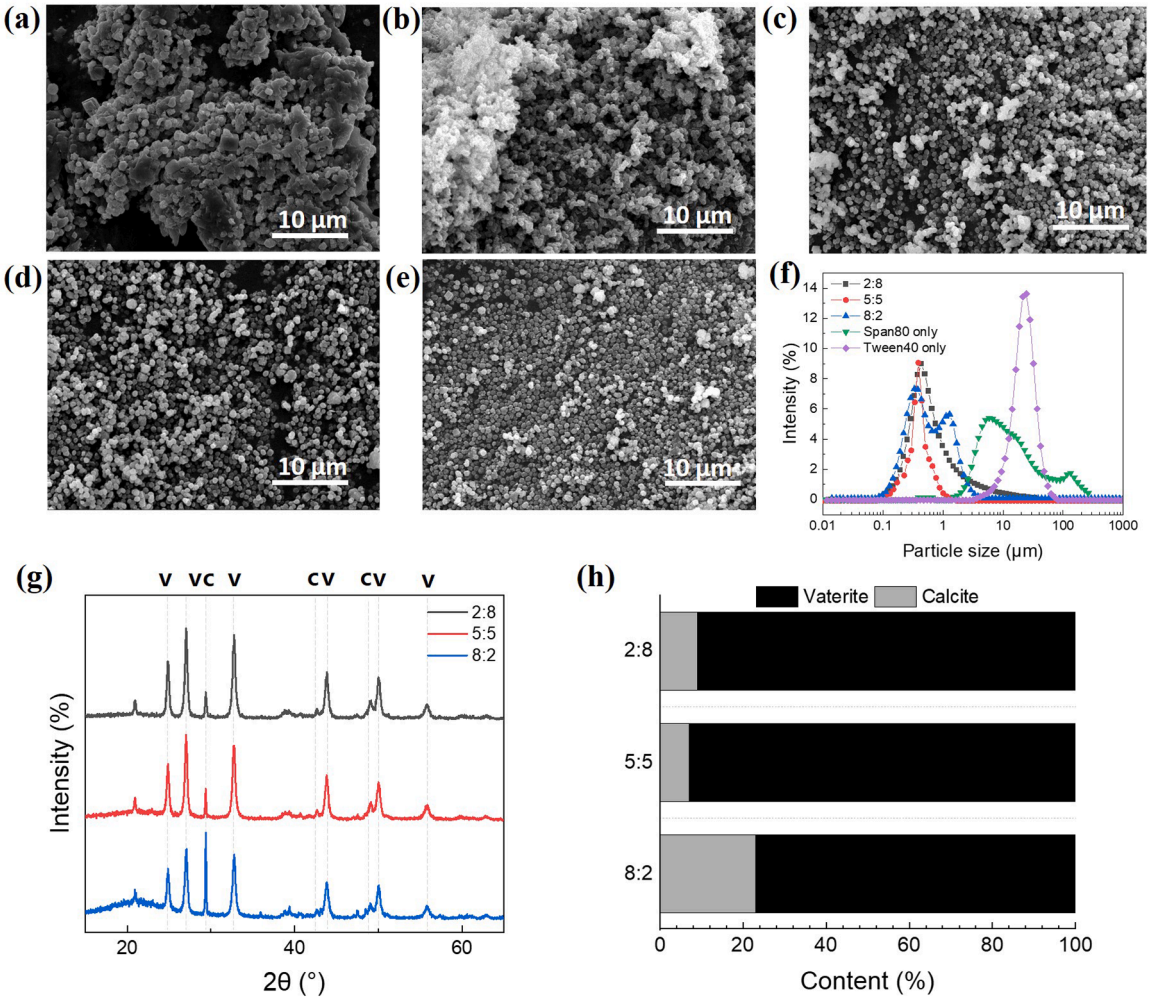

Fig. 4. Characterization of $CaCO_3$ particles synthesized with different surfactant ratios (Span 80:Tween 40). (a-e) SEM images): (a) Span 80 only, (b) Tween 40 only, (c) 2:8, (d) 8:2, and (e) 5:5. (f) Particle size distributions. (g) XRD patterns and (h) phase contents.

growth, and aggregation, providing the most favorable outcome at a 5:5 ratio (Fig. 5).

Figs. 4.(g) and (h) show the XRD patterns and phase contents of $CaCO_3$ according to the Span 80:Tween 40 ratio. At a high ratio of Tween 40 (Span 80:Tween 40 = 2:8), the vaterite phase increased significantly to 91%. This is attributed to the hydrophilic polyoxyethylene chains of Tween 40, which promote uniform ion dispersion and rapid nucleation. In addition, the hydrophobic chains of Span 80 suppressed further growth via adsorption onto the particle surface. At a 5:5 ratio, the highest vaterite content of 93% was achieved among all conditions, which was 11% higher than that of $CaCO_3$ synthesized without surfactants. A higher ratio of Span 80 (Span 80:Tween 40 = 8:2) reduced the vaterite content to 66%. Under these conditions, insufficient hydrophilic interactions in the aqueous phase hindered both nucleation and growth, leading to the formation of a calcite phase. Overall, controlling the Span 80:Tween 40 ratio influenced not only the particle size and distribution but also the crystalline phase. These findings were consistent with the SEM, DLS, and XRD results (Fig. 4). Thus, the combination of Span 80 and Tween 40 in a 5:5 ratio produced the highest vaterite content and the smallest and most uniform $CaCO_3$ nanoparticles.

3.2. *Characterization and OVA adsorption behavior of $CaCO_3$ nanoparticles*

The OVA adsorption efficiency of three different $CaCO_3$ particles was evaluated: (i) pristine $CaCO_3$, (ii) $CaCO_3$ synthesized with 1 mL of propanol, and (iii) $CaCO_3$ prepared with both 1 mL of propanol and 100 μL of a Span 80:Tween 40 mixture (5:5), as shown in Fig. 6(a). OVA adsorption was performed for 12 h, during which the adsorption efficiency reached saturation, as shown in Figure S8. The $CaCO_3$ nanoparticles maintained their size, crystal structure, and morphology even after prolonged exposure to an aqueous environment during OVA adsorption (Figure S9) and storage for a week in PBS (Figure S10).

The pristine $CaCO_3$ synthesized in an aqueous medium without additives predominantly consisted of large calcite particles with sizes of 3–5 μm (Figs. 1(a), (g), (i), and (j)) and exhibited a low adsorption efficiency of 29.4%. The $CaCO_3$ synthesized with propanol formed vaterite nanoparticles with diameters of 400 nm (Figs. 3(b), (e), (f), and (g)), and its adsorption efficiency markedly increased to 82.6%. The $CaCO_3$ prepared with both surfactant and propanol produced the smallest and most uniform vaterite nanoparticles (Figs. 4(e), (g), and (h)), resulting in the highest adsorption efficiency of 99.1%.

This trend clearly indicates that the particle size and crystal phase significantly affect OVA adsorption efficiency. Smaller, more uniform vaterite nanoparticles exhibited larger specific surface areas and more accessible adsorption sites [60]. Further characterization of $CaCO_3$ and OVA@$CaCO_3$ was performed using nanoparticles prepared with 1 mL of propanol and 100 μL of a surfactant mixture (Span 80:Tween 40 = 5:5), which were denoted as $CaCO_3$_P1_ST55 (P1: 1 mL propanol; ST55: Span 80/Tween 40 = 5:5).

Fig. 6. (a) OVA adsorption efficiencies (n = 3) of (i) pristine $CaCO_3$,

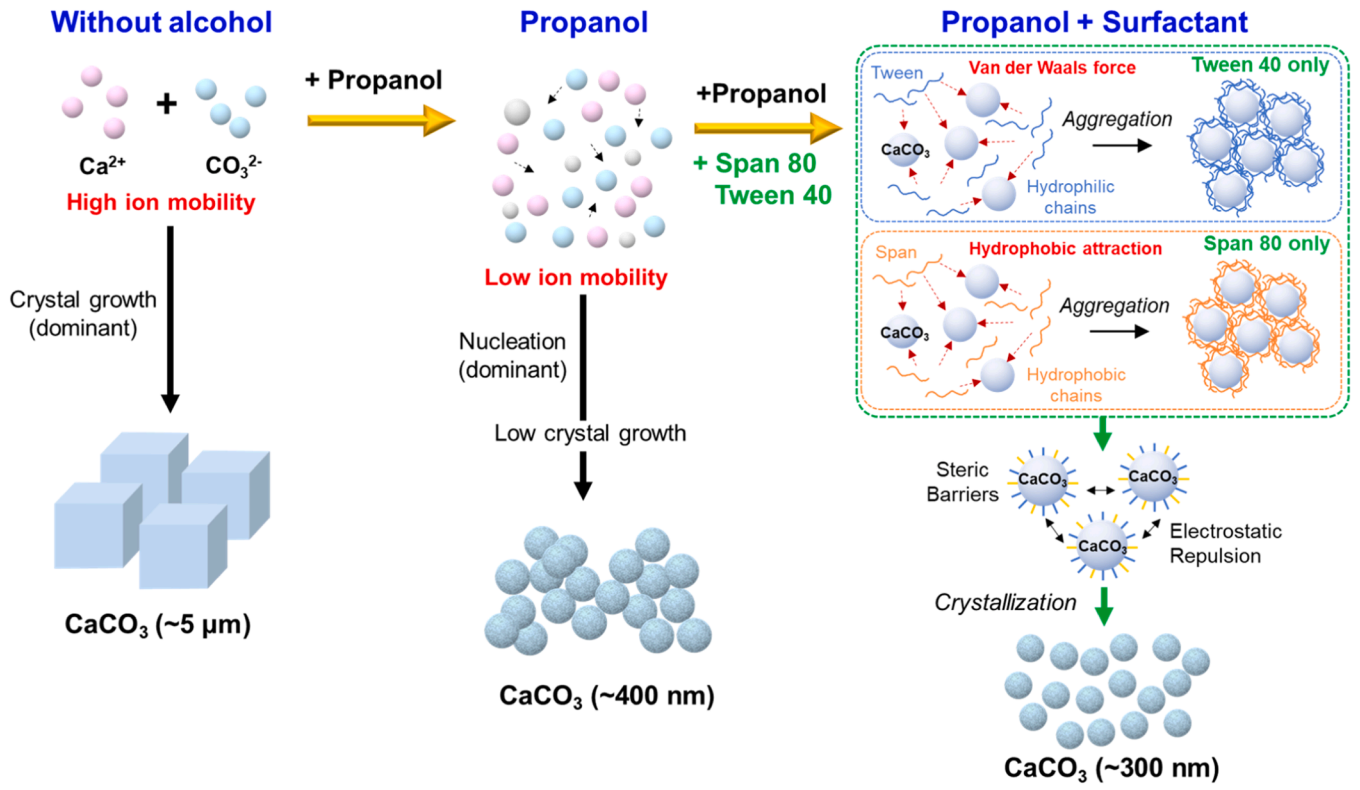

Fig. 5. Schematic of the $CaCO_3$ synthesis mechanism with different additives (alcohols and surfactants).

(ii) $CaCO_3$ synthesized with 1 mL of propanol, and (iii) $CaCO_3$ prepared with both 1 mL of propanol and 100 μL of a Span 80:Tween 40 mixture (5:5) ($CaCO_3$_P1_ST55). (b-e) Characterization of $CaCO_3$_P1_ST55 nanoparticles: (b) SEM image, (c) TEM image, (d) EDS elemental mapping, and (e) N_2 adsorption–desorption isotherm. (f–h) Characterization of OVA, pristine $CaCO_3$, and OVA@$CaCO_3$ nanoparticles: (f) FT-IR spectra, (g) zeta potential (n = 3), and (h) TGA curve.

Figs. 6(b) and (c) present high-resolution SEM and TEM images of $CaCO_3$_P1_ST55 nanoparticles. The nanoparticles had a spherical and porous structure with a diameter of 300 nm. The TEM images reveal a highly porous structure composed of numerous nanocrystalline domains, which is consistent with the typical structural features of vaterite $CaCO_3$ [60]. This porous structure provided a large surface area and internal voids, making it advantageous for drug loading and controlled drug release. Fig. 6(d) shows the SEM image and corresponding EDS elemental mapping of the $CaCO_3$ nanoparticles. The EDS maps reveal a homogeneous spatial distribution of C (blue, the large amount of blue color in the blank area is due to carbon tape), O (green), and Ca (yellow) across the entire particle, indicating the uniform chemical composition of the $CaCO_3$ nanoparticles without noticeable composition differences.

Fig. 6(e) shows the nitrogen adsorption–desorption isotherm and pore size of the $CaCO_3$ nanoparticles. In general, $CaCO_3$ prepared via the emulsion method exhibits a BET surface area of 20–57 m^2/g, whereas that synthesized via the co-precipitation method exhibits a BET surface area of ~10 m^2/g [61,62]. In this study, $CaCO_3$ nanoparticles synthesized via co-precipitation with alcohol and surfactants exhibited a far higher BET surface area of 89.3 m^2/g, attributed to the formation of highly porous nanoparticles. The adsorption–desorption isotherm displayed a typical type IV curve according to IUPAC classification, with a distinct hysteresis loop observed at relative pressures (P/P_0) of approximately 0.8–1.0. The average pore size was 26.8 nm, indicating a mesoporous structure.

Fig. 6(f) presents the FT-IR spectra of OVA, $CaCO_3$ nanoparticles, and OVA@$CaCO_3$. The OVA spectrum exhibited peaks at 3300 and 1750 cm^{-1} , corresponding to -NH/-OH groups and C═O stretching in peptide bonds, respectively. The $CaCO_3$ spectrum exhibited a strong band at 1400–1500 cm^{-1} , attributed to the asymmetric stretching of CO_3^{2-} ions. Peaks at 870 and 745 cm^{-1} were assigned to out-of-plane and in-plane bending modes, respectively, representing the vaterite fingerprint region, while the calcite-specific peak at 713 cm^{-1} appeared weak. For OVA@$CaCO_3$, the vaterite peaks remained strong. In addition, OVA peaks at 3300 cm^{-1} (–NH and –OH) and 1750 cm^{-1} (C═O) newly appeared along with an amide II band at 1540–1650 cm^{-1} (–NH bending and C–N stretching). These results indicated that OVA was stably adsorbed on the surface of the $CaCO_3$ nanoparticles while preserving the vaterite phase.

Fig. 6(g) shows the zeta potential of the synthesized $CaCO_3$ nanoparticles, which exhibited a positive surface potential of + 20.56 mV. This positive charge is commonly observed for $CaCO_3$ owing to the high hydration stability of Ca^{2+} ions [63]. After OVA adsorption, the zeta potential shifted to a negative value of –5.08 mV. This change indicated that the negatively charged OVA was uniformly adsorbed and exposed on the surface of the $CaCO_3$ nanoparticles (Figure S11), which was consistent with the FT-IR results (Fig. 6(f)).

Fig. 6(h) presents the thermal decomposition behavior of $CaCO_3$ and OVA@$CaCO_3$ determined via TGA. $CaCO_3$ exhibited major weight loss above 800 °C, corresponding to its decomposition into CaO and CO_2 [21]. In contrast, OVA@$CaCO_3$ exhibited an additional weight loss between 200 and 400 °C. Approximately 15% of the weight loss was attributed to OVA degradation, confirming the high adsorption capacity of OVA on the synthesized porous $CaCO_3$ nanoparticles.

3.3. In vitro cytotoxicity and antigen presentation of OVA@$CaCO_3$ nanoparticles

Biocompatibility is a critical factor in the utilization of nanoparticles as antigen delivery vehicles. Therefore, the cytotoxicity of the nanoparticles was evaluated.

The cytotoxicity of $CaCO_3$_P1_ST55 was assessed at various OVA concentrations using the CCK-8 assay, as shown in Fig. 7(a). The cell

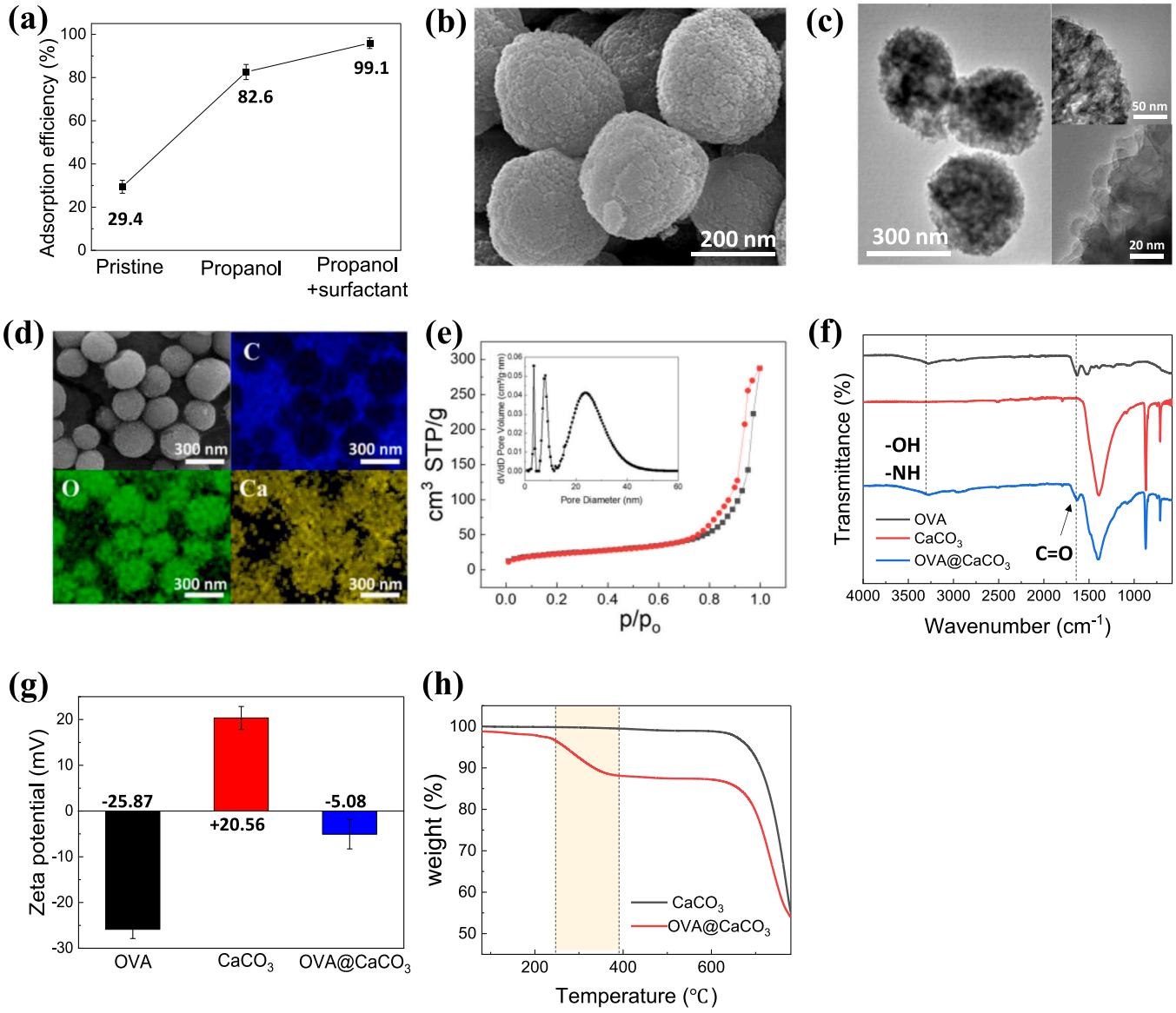

Fig. 6. (a) OVA adsorption efficiencies (n = 3) of (i) pristine $CaCO_3$, (ii) $CaCO_3$ synthesized with 1 mL of propanol, and (iii) $CaCO_3$ prepared with both 1 mL of propanol and 100 μL of a Span 80:Tween 40 mixture (5:5) ($CaCO_3$_P1_ST55). (b-e) Characterization of $CaCO_3$_P1_ST55 nanoparticles: (b) SEM image, (c) TEM image, (d) EDS elemental mapping, and (e) N_2 adsorption–desorption isotherm. (f–h) Characterization of OVA, pristine $CaCO_3$, and OVA@$CaCO_3$ nanoparticles: (f) FT-IR spectra, (g) zeta potential (n = 3), and (h) TGA curve.

viability in the range of 4–2 mg/mL was determined to be 70–80%, whereas concentrations of ≥ 1 mg/mL exhibited cell viabilities exceeding 90%. OVA itself is widely recognized as a non-cytotoxic model antigen, and previous studies have consistently demonstrated that OVA does not induce measurable cytotoxicity in commonly used immune or epithelial cell lines within typical experimental concentration ranges [64,65]

Fig. 7(b) presents the evaluation of the antigen-presentation capability through dendritic cells based on the analysis of interleukin-2 (IL-2)—a marker of T-cell activation. Antigen cross-presentation refers to the process whereby exogenous antigens phagocytosed by dendritic cells are presented via MHC class I molecules, leading to the activation of CD8 + T cells that recognize the presented antigen and subsequently secrete cytokines, such as IL-2. Therefore, high IL-2 secretion by CD8 + T cells indicates a larger number of phagocytosed antigens. In this study, the antigen-presentation ability of nanoparticles in dendritic cells was evaluated by measuring IL-2 secreted by CD8 + OVA-specific T cells.

IL-2 secretion reached its maximum level at an OVA concentration of 1 mg/mL (~2200 pg/mL) and then decreased in a concentration-dependent manner. At concentrations of 4 and 2 mg/mL, IL-2 secretion was lower than that at 1 mg/mL. This result was consistent with the cytotoxicity observations. Some dendritic cells exposed to higher nanoparticle concentrations experienced cytotoxicity and cell death, leading to reduced phagocytosis compared with the 1-mg/mL concentration (Figure S12).

Notably, the $CaCO_3$ nanoparticles enhanced antigen uptake and subsequent presentation without inducing significant cytotoxicity, thereby exhibiting an adjuvant-like effect mediated by improved antigen delivery rather than direct immunostimulation. Accordingly, cytotoxicity evaluation was conducted using dendritic cells instead of cancer or epithelial cell lines, as dendritic cells represent the most relevant model for assessing the safety and functionality of vaccine-oriented antigen delivery systems.

Overall, treatment of dendritic cells with $CaCO_3$ nanoparticles at concentrations of ≤ 1 mg/mL resulted in negligible cytotoxicity while

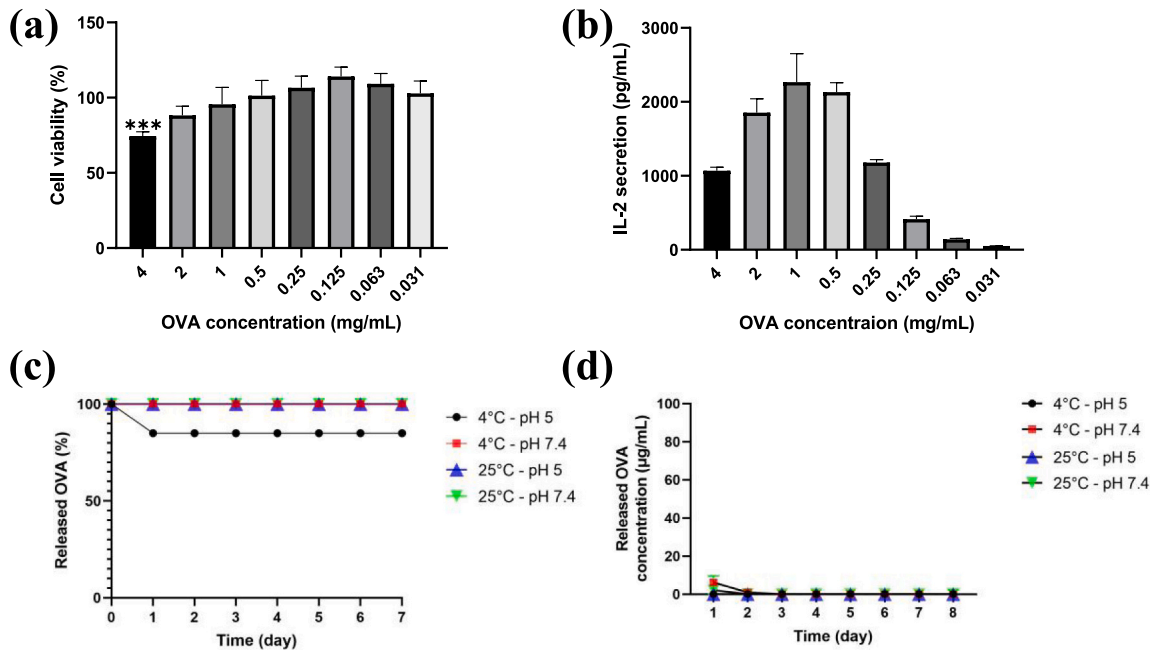

Fig. 7. (a) Cytotoxicity of OVA@$CaCO_3$ nanoparticles evaluated via the CCK-8 assay, (b) IL-2 secretion from T-cells upon antigen presentation, (c) Time-dependent OVA release ratio under different pH (5.0 and 7.4) and temperature (4 °C and 25 °C) conditions, and (d) OVA release concentration as a function of time (Data are presented as mean ± standard deviation (n = 3)).

maintaining excellent antigen-presentation capability. These results demonstrate the biocompatibility of the nanoparticles and their effectiveness in antigen loading and presentation, highlighting the advantages of $CaCO_3$-based nanoparticle systems for vaccine-oriented applications.

Figs. 7(c) and (d) present the time-dependent OVA release behavior from OVA@$CaCO_3$ nanoparticles under different pH (5.0 and 7.4) and temperature (4 and 25 °C) conditions. Across all tested conditions, no substantial release of OVA was observed over the 7-day period. A slight release was detected only on day 1, and this trend was consistently reproduced in three independent experiments. After the initial time point, the released OVA level remained close to zero, indicating negligible further release. This minimal and transient release suggests that a small fraction of weakly bound or surface-associated OVA may be released during the initial equilibration stage at the condition (4℃ and pH 5), whereas the majority of OVA remains strongly retained within the $CaCO_3$ carrier. This result suggests that OVA remained strongly bound to the $CaCO_3$ carrier due to the high adsorption affinity between the two materials. Consistent with this observation, zeta potential measurements (Fig. 6(g)) revealed that OVA alone exhibited a value of –25.87 mV, $CaCO_3$ showed + 20.56 mV, and the OVA@$CaCO_3$ complex presented –5.08 mV, confirming strong electrostatic interactions between them. Such strong binding implies that the $CaCO_3$-based material developed in this study provides stable antigen retention and effective antigen presentation, demonstrating its potential as a robust vaccine adjuvant.

4. Conclusions

In this study, porous vaterite $CaCO_3$ nanoparticles were successfully synthesized via an alcohol–surfactant-assisted co-precipitation method. The combined use of alcohols and nonionic surfactants enabled precise control over ion diffusion, nucleation, and crystal growth, leading to uniform vaterite nanoparticles with an average size of ~300 nm and high specific surface area. Systematic investigation revealed that solvent polarity, viscosity, and surfactant HLB balance play critical roles in stabilizing the metastable vaterite phase and suppressing particle aggregation.

The optimized $CaCO_3$ nanoparticles exhibited excellent OVA adsorption efficiency (>99%) and pH/temperature-responsive release behavior. In vitro evaluations using dendritic cells demonstrated high biocompatibility and enhanced antigen-presentation capability, indicating an adjuvant-like effect mediated by improved antigen delivery. Overall, this work presents a simple and scalable strategy for engineering stable, porous vaterite $CaCO_3$ nanoparticles, highlighting their potential as versatile carriers for antigen delivery and other biomedical applications.

CRediT authorship contribution statement

Seong-Joong Kim: Writing – review & editing, Writing – original draft, Supervision, Conceptualization. **Min-Kyung Kang:** Writing – review & editing, Writing – original draft, Methodology. **A-Ran Min:** Visualization, Data curation. **Jin-Woo Jeong:** Formal analysis, Data curation. **A-Jin Kim:** Validation, Methodology, Formal analysis. **Chansu Park:** Methodology, Formal analysis. **Kangwon Lee:** Writing – review & editing, Supervision, Investigation. **Young-Ran Lee:** Writing – review & editing, Writing – original draft, Supervision, Funding acquisition, Conceptualization. **Seung-Yeon Kim:** Writing – review & editing, Writing – original draft, Methodology, Investigation.

Declaration of Competing Interest

The authors declare that they have no known competing financial interests or personal relationships that could have appeared to influence the work reported in this paper.

Acknowledgments

This research was supported by The Government-wide R&D to Advance Infectious Disease Prevention and Control, Republic of Korea (grant number: RS-2023-KH140358), the Korea Institute of Ceramic Engineering and Technology (KICET, 2410013749), and the National Research Council of Science & Technology (NST) grant by the Korea government (MSIP) (No. CRC22043–300).

Appendix A. Supporting information

Supplementary data associated with this article can be found in the online version at doi:10.1016/j.colsurfb.2026.115592.

Data Availability

Data will be made available on request.

References

[1] L. Biny, E. Gerasimovich, A. Karaulov, A. Sukhanova, I. Nabiev, Functionalized calcium carbonate-based microparticles as a versatile tool for targeted drug delivery and cancer treatment, Pharmaceutics 16 (2024) 653.

[2] A. Wang, Y. Yang, X. Zhang, X. Liu, W. Cui, J. Li, Gelatin-Assisted synthesis of vaterite nanoparticles with higher surface area and porosity as anticancer drug containers in vitro, ChemPlusChem 81 (2016) 194–201.

[3] V.K. Popova, D.V. Pyshnyi, E.V. Dmitrienko, Biomedical applications of calcium carbonate nanoparticles: a review of recent advances, ACS Biomater. Sci. & Eng. 11 (2025) 6359–6385.

[4] X. Deng, Z. Yang, K.W. Chan, N. Ismail, M.Z. Abu Bakar, 5-fluorouracil in combination with calcium carbonate nanoparticles loaded with antioxidant thymoquinone against colon cancer: synergistically therapeutic potential and underlying molecular mechanism, Antioxidants 13 (2024) 1030.

[5] D.B. Trushina, T.N. Borodina, S. Belyakov, M.N. Antipina, Calcium carbonate vaterite particles for drug delivery: advances and challenges, Mater. Today Adv. 14 (2022) 100214.

[6] M.H. Azarian, W. Sutapun, Biogenic calcium carbonate derived from waste shells for advanced material applications: a review, Front. Mater. 9 (2022) 1024977.

[7] A. Mandal, Scope of $CaCO_3$-based nanohybrids for environmental and biomedical applications: state of the art, recent advances, and future perspectives, Rev. Environ. Sci. Bio/Technol. 24 (2025) 911–955.

[8] C. Xu, Y. Yan, J. Tan, D. Yang, X. Jia, L. Wang, Y. Xu, S. Cao, S. Sun, Biodegradable nanoparticles of polyacrylic acid–stabilized amorphous $CaCO_3$ for tunable pH-responsive drug delivery and enhanced tumor inhibition, Adv. Funct. Mater. 29 (2019) 1808146.

[9] Q. Zhong, W. Li, X. Su, G. Li, Y. Zhou, S.C. Kundu, J. Yao, Y. Cai, Degradation pattern of porous $CaCO_3$ and hydroxyapatite microspheres in vitro and in vivo for potential application in bone tissue engineering, Colloids Surf. B Biointerfaces 143 (2016) 56–63.

[10] Y. Huang, L. Cao, B.V. Parakhonskiy, A.G. Skirtach, Hard, soft, and hard-and-soft drug delivery carriers based on $CaCO_3$ and alginate biomaterials: synthesis, properties, pharmaceutical applications, Pharmaceutics 14 (2022) 909.

[11] S. Maleki Dizaj, M. Barzegar-Jalali, M.H. Zarrintan, K. Adibkia, F. Lotfipour, Calcium carbonate nanoparticles as cancer drug delivery system, Expert Opin. Drug Deliv. 12 (2015) 1649–1660.

[12] S. Maleki Dizaj, S. Sharifi, E. Ahmadian, A. Eftekhari, K. Adibkia, F. Lotfipour, An update on calcium carbonate nanoparticles as cancer drug/gene delivery system, Expert Opin. Drug Deliv. 16 (2019) 331–345.

[13] C. Qi, S. Musetti, L.-H. Fu, Y.-J. Zhu, L. Huang, Biomolecule-assisted green synthesis of nanostructured calcium phosphates and their biomedical applications, Chem. Soc. Rev. 48 (2019) 2698–2737.

[14] W. Li, Z. Cao, R. Liu, L. Liu, H. Li, X. Li, Y. Chen, C. Lu, Y. Liu, AuNPs as an important inorganic nanoparticle applied in drug carrier systems, Artif. Cells Nanomed. Biotechnol. 47 (2019) 4222–4233.

[15] S. Chen, X. Hao, X. Liang, Q. Zhang, C. Zhang, G. Zhou, S. Shen, G. Jia, J. Zhang, Inorganic nanomaterials as carriers for drug delivery, J. Biomed. Nanotechnol. 12 (2016) 1–27.

[16] Y.T. Lim, O.O. Park, H.-T. Jung, Gold nanolayer-encapsulated silica particles synthesized by surface seeding and shell growing method: near infrared responsive materials, J. Colloid Interface Sci. 263 (2003) 449–453.

[17] S. Punj, J. Singh, K. Singh, Ceramic biomaterials: properties, state of the art and future prospectives, Ceram. Int. 47 (2021) 28059–28074.

[18] S.V. Dorozhkin, Biocomposites and hybrid biomaterials based on calcium orthophosphates, Biomatter 1 (2011) 3–56.

[19] S. Van Rijt, K. De Groot, S.C. Leeuwenburgh, Calcium phosphate and silicate-based nanoparticles: history and emerging trends, Tissue Eng. Part A 28 (2022) 461–477.

[20] A.D. Trofimov, A.A. Ivanova, M.V. Zyuzin, A.S. Timin, Porous inorganic carriers based on silica, calcium carbonate and calcium phosphate for controlled/modulated drug delivery: fresh outlook and future perspectives, Pharmaceutics 10 (2018) 167.

[21] Y.-Q. Niu, J.-H. Liu, C. Aymonier, S. Fermani, D. Kralj, G. Falini, C.-H. Zhou, Calcium carbonate: controlled synthesis, surface functionalization, and nanostructured materials, Chem. Soc. Rev. 51 (2022) 7883–7943.

[22] P.N. Gavryushkin, A.B. Belonoshko, N. Sagatov, D. Sagatova, E. Zhitova, M. G. Krzhizhanovskaya, A. Recnik, E.V. Alexandrov, I.V. Medrish, Z.I. Popov, Metastable structures of $CaCO_3$ and their role in transformation of calcite to aragonite and postaragonite, Cryst. Growth & Des. 21 (2020) 65–74.

[23] Y. Huang, A.G. Skirtach, B.V. Parakhonskiy, Systematic study of stability, loading efficiency and release mechanisms, and cellular interaction of vaterite with various sizes, Ceram. Int. 50 (2024) 7469–7479.

[24] H. Bahrom, A.A. Goncharenko, L.I. Fatkhutdinova, O.O. Peltek, A.R. Muslimov, O. Y. Koval, I.E. Eliseev, A. Manchev, D. Gorin, I.I. Shishkin, Controllable synthesis of calcium carbonate with different geometry: comprehensive analysis of particles formation, their cellular uptake and biocompatibility, ACS Sustain. Chem. & Eng. 7 (2019) 19142–19156.

[25] N. Spanos, P.G. Koutsoukos, The transformation of vaterite to calcite: effect of the conditions of the solutions in contact with the mineral phase, J. Cryst. Growth 191 (1998) 783–790.

[26] G.-T. Zhou, Q.-Z. Yao, S.-Q. Fu, Y.-B. Guan, Controlled crystallization of unstable vaterite with distinct morphologies and their polymorphic transition to stable calcite, Eur. J. Mineral. 22 (2010) 259–269.

[27] S. Gill, R. Löbenberg, T. Ku, S. Azarmi, W. Roa, E.J. Prenner, Nanoparticles: characteristics, mechanisms of action, and toxicity in pulmonary drug delivery—a review, J. Biomed. Nanotechnol. 3 (2007) 107–119.

[28] X. Yang, Y. Sun, H. Zhang, F. Liu, Q. Chen, Q. Shen, Z. Kong, Q. Wei, J.-W. Shen, Y. Guo, $CaCO_3$ nanoplatform for cancer treatment: drug delivery and combination therapy, Nanoscale 16 (2024) 6876–6899.

[29] N.M. Palmqvist, J.-M. Nedelec, G.A. Seisenbaeva, V.G. Kessler, Controlling nucleation and growth of nano-$CaCO_3$ via CO_2 sequestration by a calcium alkoxide solution to produce nanocomposites for drug delivery applications, Acta Biomater. 57 (2017) 426–434.

[30] M. Nassar, T. Farrag, M. Mahmoud, S. Abdelmonem, K.A. Khalil, N.A. Barakat, Influence of the operating conditions on the morphology of $CaCO_3$ nanoparticles prepared by modified co-precipitation with pulse mode feeding, Adv. Powder Technol. 26 (2015) 914–919.

[31] X. Guo, X. Li, L. Chan, W. Huang, T. Chen, Edible $CaCO_3$ nanoparticles stabilized Pickering emulsion as calcium-fortified formulation, J. Nanobiotechnol. 19 (2021) 67.

[32] V. Mavromatis, V. Montouillout, J. Noireaux, J. Gaillardet, J. Schott, Characterization of boron incorporation and speciation in calcite and aragonite from co-precipitation experiments under controlled pH, temperature and precipitation rate, Geochim. Et. Cosmochim. Acta 150 (2015) 299–313.

[33] Z. Sun, S. Luo, P. Qi, L.-S. Fan, Ionic diffusion through Calcite ($CaCO_3$) layer during the reaction of CaO and CO_2, Chem. Eng. Sci. 81 (2012) 164–168.

[34] R. Zhang, L. Yang, R. Tu, J. Huo, J. Wang, J. Zhou, D. Chen, Emulsion phase inversion from oil-in-water (1) to water-in-oil to oil-in-water (2) induced by in situ surface activation of $CaCO_3$ nanoparticles via adsorption of sodium stearate, Colloids Surf. A Physicochem. Eng. Asp. 477 (2015) 55–62.

[35] C. Lin, M. Akhtar, Y. Li, M. Ji, R. Huang, Recent developments in $CaCO_3$ Nano-Drug Delivery systems: advancing biomedicine in tumor diagnosis and treatment, Pharmaceutics 16 (2024) 275.

[36] L. Xiang, Y. Xiang, Y. Wen, F. Wei, Formation of $CaCO_3$ nanoparticles in the presence of terpineol, Mater. Lett. 58 (2004) 959–965.

[37] F. Persano, C. Nobile, C. Piccirillo, G. Gigli, S. Leporatti, Monodisperse and nanometric-sized calcium carbonate particles synthesis optimization, Nanomaterials 12 (2022) 1494.

[38] D.B. Trushina, T.V. Bukreeva, M.N. Antipina, Size-controlled synthesis of vaterite calcium carbonate by the mixing method: aiming for nanosized particles, Cryst. Growth & Des. 16 (2016) 1311–1319.

[39] X.H. Guo, S.H. Yu, G.B. Cai, Crystallization in a mixture of solvents by using a crystal modifier: morphology control in the synthesis of highly monodisperse $CaCO_3$ microspheres, Angew. Chem. Int. Ed. 45 (2006) 3977–3981.

[40] D. Konopacka-Łyskawa, Synthesis methods and favorable conditions for spherical vaterite precipitation: a review, Crystals 9 (2019) 223.

[41] Y. Mori, T. Enomae, A. Isogai, Preparation of pure vaterite by simple mechanical mixing of two aqueous salt solutions, Mater. Sci. Eng. C 29 (2009) 1409–1414.

[42] F.W. Yan, S.F. Zhang, C.Y. Guo, X.H. Zhang, G.C. Chen, F. Yan, G.Q. Yuan, Influence of stirring speed on the crystallization of calcium carbonate, Cryst. Res. Technol. 44 (2009) 725–728.

[43] M.D. Daud, A.N. Hashim, A. Rahmat, M.M. Al Bakri Abdullah, A.H.I. Jalauddin, Control of the crystal morphological characteristic and size of nano-PCC via turbo-mixing reactive precipitation, Appl. Mech. Mater. 754 (2015) 770–774.

[44] D. Trushina, S. Sulyanov, T. Bukreeva, M. Kovalchuk, Size control and structure features of spherical calcium carbonate particles, Crystallogr. Rep. 60 (2015) 570–577.

[45] I.W. Kim, R.E. Robertson, R. Zand, Effects of some nonionic polymeric additives on the crystallization of calcium carbonate, Cryst. Growth & Des. 5 (2005) 513–522.

[46] G. Yan, L. Wang, J. Huang, The crystallization behavior of calcium carbonate in ethanol/water solution containing mixed nonionic/anionic surfactants, Powder Technol. 192 (2009) 58–64.

[47] J.-J. Qi, M.-H. Liu, L. He, J.-X. Wang, X.-F. Zeng, A general strategy for controllable preparation of nano-$CaCO_3$, Langmuir 41 (2024) 1137–1148.

[48] D. Konopacka-Łyskawa, B. Kościelska, J. Karczewski, Controlling the size and morphology of precipitated calcite particles by the selection of solvent composition, J. Cryst. Growth 478 (2017) 102–110.

[49] D. Konopacka-Łyskawa, B. Kościelska, J. Karczewski, Effect of some organic solvent–water mixtures composition on precipitated calcium carbonate in carbonation process, J. Cryst. Growth 418 (2015) 25–31.

[50] E.M. Flaten, M. Seiersten, J.-P. Andreassen, Polymorphism and morphology of calcium carbonate precipitated in mixed solvents of ethylene glycol and water, J. Cryst. Growth 311 (2009) 3533–3538.

[51] L. Zhang, L.-H. Yue, F. Wang, Q. Wang, Divisive effect of alcohol– water mixed solvents on growth morphology of calcium carbonate crystals, J. Phys. Chem. B 112 (2008) 10668–10674.

[52] G. Magnabosco, I. Polishchuk, B. Pokroy, R. Rosenberg, H. Cölfen, G. Falini, Synthesis of calcium carbonate in trace water environments, Chem. Commun. 53 (2017) 4811–4814.

[53] H. Du, E. Amstad, Water: How does it influence the $CaCO_3$ formation? Angew. Chem. Int. Ed. 59 (2020) 1798–1816.
[54] J.F. Rodríguez, A. de Lucas, J.R. Leal, J.L. Valverde, Determination of intraparticle diffusivities of Na^+/K^+ in water and water/alcohol mixed solvents on a strong acid cation exchanger, Ind. & Eng. Chem. Res. 41 (2002) 3019–3027.
[55] E.M. Pouget, P.H. Bomans, J.A. Goos, P.M. Frederik, G. de With, N.A. Sommerdijk, The initial stages of template-controlled $CaCO_3$ formation revealed by cryo-TEM, Science 323 (2009) 1455–1458.
[56] C. Bus, M. Kocsis, A. Agoston, A. Kukovecz, Z. Konya, P. Sipos, Application of alcohols to inhibit the formation of Ca(II) Dodecyl sulfate precipitate in aqueous solutions, Mater. (Basel) 17 (2024).
[57] S. Veesler, E. Revalor, O. Bottini, C. Hoff, Crystallization in the presence of a liquid− liquid phase separation, Org. Process Res. & Dev. 10 (2006) 841–845.
[58] Z.G. Cui, Y.Z. Cui, C.F. Cui, Z. Chen, B.P. Binks, Aqueous foams stabilized by in situ surface activation of $CaCO_3$ nanoparticles via adsorption of anionic surfactant, Langmuir 26 (2010) 12567–12574.
[59] E. Song, D. Kim, B.J. Kim, J. Lim, Surface modification of $CaCO_3$ nanoparticles by alkylbenzene sulfonic acid surfactant, Colloids Surf. A Physicochem. Eng. Asp. 461 (2014) 1–10.
[60] N. Zhang, B. Zhao, P. Yang, H. Zhang, Systematic study of preparing porous $CaCO_3$ vaterite particles for controlled drug release, Nanomaterials 15 (2025) 1227.
[61] J.-H. Yang, S.-M. Shih, C.-I. Wu, C.Y.-D. Tai, Preparation of high surface area $CaCO_3$ for SO_2 removal by absorption of CO_2 in aqueous suspensions of $Ca(OH)_2$, Powder Technol. 202 (2010) 101–110.
[62] C. Affolter-Zbaraszczuk, H. Ozcelik, F. Meyer, O. Gallet, P. Lavalle, V. Ball, C. M. Ghimbeu, P. Schaaf, H. Knopf-Marques, Hybrid extracellular matrix microspheres for development of complex multicellular architectures, RSC Adv. 7 (2017) 5528–5532.
[63] J. Song, Y. Zeng, L. Wang, X. Duan, M. Puerto, W.G. Chapman, S.L. Biswal, G. J. Hirasaki, Surface complexation modeling of calcite zeta potential measurements in brines with mixed potential determining ions (Ca^{2+}, CO_3^{2-}, Mg^{2+}, SO_4^{2-}) for characterizing carbonate wettability, J. Colloid Interface Sci. 506 (2017) 169–179.
[64] K.L. Rock, S. Gamble, L. Rothstein, Presentation of exogenous antigen with class I major histocompatibility complex molecules, Science 249 (1990) 918–921.
[65] W. Jiang, B.Y. Kim, J.T. Rutka, W.C. Chan, Nanoparticle-mediated cellular response is size-dependent, Nat. Nanotechnol. 3 (2008) 145–150 (ADDIN).